Electronic Supplementary Material

Characterization and modeling of the temperature-dependent thermal conductivity in sintered porous silicon-aluminum nanomaterials

Danny Kojda[1] (✉), Tommy Hofmann[1], Natalia Gostkowska-Lekner[1,2], and Klaus Habicht[1,2]

[1] *Department Dynamics and Transport in Quantum Materials, Helmholtz-Zentrum Berlin für Materialien und Energie GmbH, Berlin D-14109, Germany*
[2] *Institute of Physics and Astronomy, University of Potsdam, Potsdam D-14476, Germany*

Section S1 Quantitative image analysis

SEM images are analyzed by algorithms to extract the domain size distributions as well as interpore distance distributions with high sampling numbers. Finding domains of individual grains in a pixeled gray scale image can be classified as image segmentation problem, which is a vast topic. In our SEM images, differently oriented grains show a different contrast due to the channeling effect. Even at maximum contrast of the SEM, the contrast between different grains is very low, so that classical approaches like edge finding algorithms or the classical watershed algorithm result in strong over/under segmentation and heavily depend on the user's supervision and on a lot of free parameters. To overcome these issues, we applied a random walker segmentation [S1] with random seeding in position and amount for a few hundred times for every image using the scikit-image packages [S2]. The calculation of the individual segmentation just needs the original image and can easily be parallelized. Nevertheless, the random walk is very expensive in computation time so that images are downsampled which may exclude smallest domains of the original image. The individual segmentations from random seeds are added to generate edge probability maps, as exemplarily shown in Fig. S1(b).
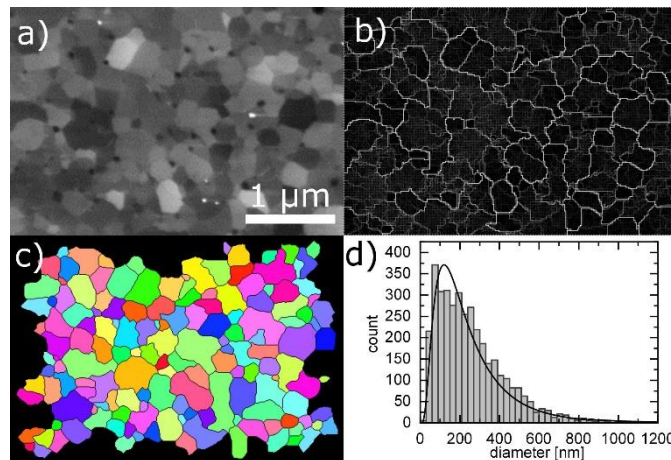

Figure S1 a) SEM image of a polished sample. b) Edge probability map of the SEM image (a) generated by multiple random walks with random seeding. c) Generated segmentation of (b) created with the MorphoLibJ package. Black separating lines are shown for clearness only. d) Histogram summarizing the diameter distribution taken from multiple SEM images. A log-normal distribution is shown as solid line.

The probability maps are further processed with Fiji/ImageJ [S3] by means of smoothing and application of an advanced watershed pipeline, that is given by the MorphoLibJ packages [S4]. The segmentation can be optimized by variation of the smoothing and the tolerance value of the MorphoLibJ package. The final segmentation is cleared at the borders as seen in Fig. S1(c). For highly porous samples, labels that can be attributed to pores were removed by applying color thresholds before further analysis (not shown in Fig. S1(c)). The areas A_i of the remaining labels i are analyzed. We introduce a mean domain size d_i as

$$d_i = 2\sqrt{\frac{A_i}{\pi}},$$

assuming that the majority of domains is circular, which is a strong simplification. The domain diameter distributions are analyzed by histograms comprising data of SEM images of the same sample taken at different magnifications. We observe, that the domain size of all samples can be described by a log-normal distribution.
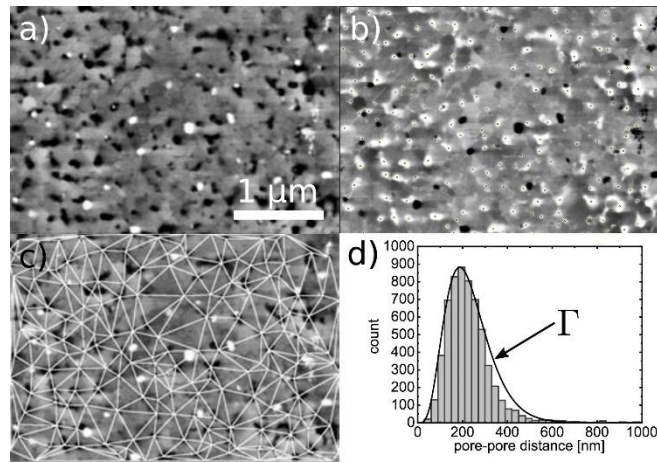
Figure S2 a) SEM image of a polished sample. b) Inverted image with marked maxima. These summits correspond to pores in the non-inverted image. c) Delaunay triangulation of the points of subfigure (b) overlaid on subfigure (a). d) Histogram summarizing the interpore distance distribution from different SEM images.

The interpore distance distribution is also extracted in an automated way. First, the *find maxima* routine of Fiji/ImageJ [S3] is applied on color inverted SEM images to identify pore positions (Fig. S2(b)). In a second step, these points are used to create a planar Delaunay triangulation (Fig. S2(c)). Every line represents an interpore distance, which is evaluated in a histogram for different images with different magnifications (Fig. S2(d)). Here, we find, that the interpore distance distribution can be described by a Γ-distribution.

Section S2 A Landauer/Lundstrom approach for thermal conductivity of nanostructured silicon

Previously, a Landauer/Lundstrom approach was successfully used to describe the thermal conductivity of bulk silicon and thin films [S5, S6]. In order to describe the temperature-dependent thermal conductivity of our nanostructured samples, we modified this model by an additional scattering term for scattering by domain boundaries of the nanostructure. Further, the relative thermal conductivity λ_r is taken into account to scale the thermal conductivity with respect to porosity.

The effective thermal conductivity λ_{eff} is

$$\lambda_{eff} = \lambda_r \lambda_0 = \lambda_r \hbar \left(\frac{k_B^2 \pi^2}{3h} T_L\right) \int_0^{\omega_0} \frac{4}{3} \Lambda(\omega) M_{ph}(\omega) W_{ph}(\omega) d\omega \qquad (1)$$

with $k_B^2 \pi^2 / 3h$ the quantum of the thermal conductance, T_L the lattice temperature, Λ the phonon mean free path, M_{ph} the number of conducting channels (modes) and W_{ph} the window function. The window function is defined as

$$W_{ph}(\omega) = \frac{3}{\pi^2 k_B T} \left(\frac{\hbar\omega}{k_B T_L}\right)^2 \left(e^{\frac{\hbar\omega}{k_B T}} - 1\right)^{-2} e^{\frac{\hbar\omega}{k_B T}}. \qquad (2)$$

The number of modes $M_{ph}(\omega)$ can be calculated from the density of states (DOS) by

$$M_{ph}(\omega) = \frac{\pi}{2} DOS(\omega) v_g(\omega), \qquad (3)$$

with v_g the phonon group velocity. To determine the DOS and $v_g(\omega)$, an isotropic sinusoidal dispersion relation is used

$$\omega = \omega_0 \sin\left(\frac{\pi}{2} \frac{q}{q_D}\right), \qquad (4)$$

with the Debye wave vector $q_D = \omega_D / v_s$. The Debye frequency is calculated by

$$\omega_D = v_s \left(6\pi^2 \frac{N}{V}\right)^{\frac{1}{3}} = v_s \left(6\pi^2 \frac{\rho_{Si}}{m_{Si}}\right)^{\frac{1}{3}}, \qquad (5)$$

using the density of silicon ρ_{Si}, the atomic mass of silicon m_{Si} and the average speed of sound v_s. For v_s the longitudinal and transverse phonon group velocities ($v_l = 8{,}433$ m/s, $v_t = 5{,}844$ m/s) for silicon [S7] are averaged as

$$v_s = \left(\frac{1}{3} \left(\frac{2}{v_t^3} + \frac{1}{v_l^3} \right) \right)^{-\frac{1}{3}}. \tag{6}$$

As consistency check, we determine the Debye temperature from $T_D = \hbar\omega_D/k_B = 697.3$ K deviating by about 9% from the literature value of 640 K.

The group velocity is

$$v_{g(\omega)} := \frac{\partial\omega}{\partial q} = \frac{\pi}{2} \frac{\omega_0}{q_D} cos\left(\frac{\pi}{2} \frac{q(\omega)}{q_D} \right), \tag{7}$$

with $q(\omega) = 2\ q_D/\pi$ arcsin (ω/ω_0) the inverse of Eq. 5. The frequency at the zone boundary ω_0 can be determined from the long wavelength limit of Eq. 8 to be $\omega_0 = 2\ v_s\ q_D/\pi = 2\ \omega_D/\pi$. Using the previous definitions, the DOS is

$$DOS(\omega) = \frac{3}{2\pi^2} \frac{q^2(\omega)}{v_g(\omega)}. \tag{8}$$

The phonon mean free path $\Lambda(\omega) = v_g(\omega)\ \tau_{tot}$ is determined by the individual scattering mechanisms whose scattering times are added by Matthiessen's rule

$$\tau_{tot} = \left(\tau_{imp}^{-1} + \tau_{boundary}^{-1} + \tau_{umklapp}^{-1} + \tau_D^{-1} \right)^{-1}. \tag{9}$$

The scattering rates for impurity scattering, boundary scattering, and Umklapp scattering are given by $\tau_{imp}^{-1} = D\omega^4$, $\tau_{boundary}^{-1} = v_g(\omega)/(F\ l)$ and $\tau_{umklapp}^{-1} = B\omega^2\ T_L\ e^{(-C/T)}$ [S6]. To introduce additional scattering by nanostructured domains, we define $\Lambda_D = v_g(\omega)\ \tau_D$ the effective mean scattering length representing a mean value that unifies scattering events at domains and pores.

Using the modified model, silicon reference data [S8] were fitted in the temperature range between 1 K and 1,000 K using the reported values for B = 2.8 x 10^{-19} s/K, C = 140 K (fixed), F = 0.4, l = 7.16 x 10^{-3} m (fixed), D = 1.32 x 10^{-45} s^3 (fixed), λ_r = 1 (fixed) and Λ_D = 10,000 m (fixed) as initial values [S6]. Best agreement was found for a reduced Umklapp scattering B = 1.54 x 10^{-19} s/K and increased F = 0.53, that were used as fixed parameters for non-linear least square fits of our measurement data.

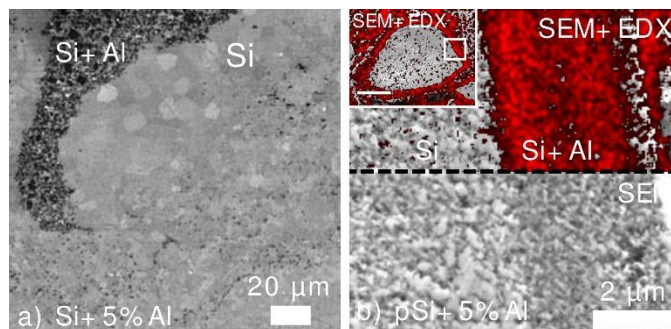## Section S3 Different effects of aluminum for powder and pSi samples

Figure S3 a) SEM micrograph of USB mixed powder sample with 5 % aluminum powder showing an agglomeration of aluminum particles as dark features. As shown, stronger grain growth appears in the vicinity of the agglomeration. b) SEM/EDX image of a USD mixed pSi sample with 5 % aluminum powder. The inset shows a combined SEM/EDX signal indicating the position of aluminum encircling a micrometer sized pSi particle. The scale bar of the inset measures 25 μm. The white box indicates the measurement position of the main image showing the SEM/EDX signal in the top image and the pure SEM signal in the bottom.

Section S4 Analysis of densification curves

Figure S4 shows the densification curves for sintered pSi samples. The onset for compaction depends on the initial porosity Φ_i and the amount of added aluminum. The higher the initial porosity, the lower the onset temperature for compaction. The fragile network of the highly porous sample pSi(IV) cracks and densifies with the applied pressure in the entire temperature range, so that the onset temperature cannot be determined.
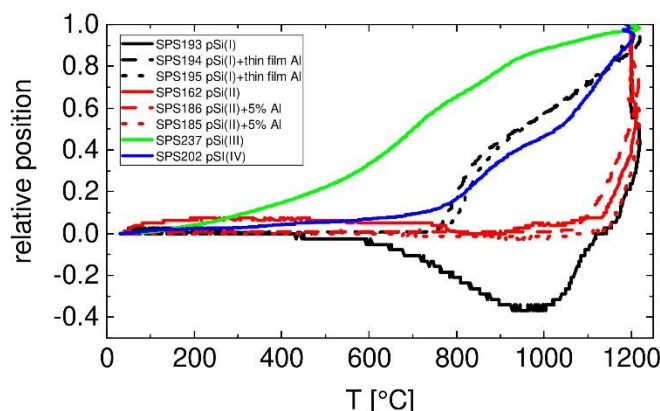

Figure S4 Relative piston position during spark plasma sintering is shown as a function of the sinter temperature for pSi samples. Positive values correspond to compaction and negative values to expansion. Negative values are caused by thermal expansion.

The sputtered aluminum film significantly reduces the onset temperature from 1,000 °C to 750 °C. For pSi(II) the added aluminum nanopowder does not affect the compaction. The aluminum diffused into individual micro meter sized grains of pSi(II) rather than building a composition of lower melting temperature (Fig. S3).

Section S5 Experimental and sample parameters

It is obvious that the experimental variables for SPS are multivariate, given by parameters such as base material, aluminum concentration, mixing types, SPS maximum temperature, and SPS holding time. Covering the full parameter space by experiments is not possible. Our experimental parameter choice is based on the results of the univariate sequence of increasing aluminum concentration (see SPS40 to SPS77 in table S1). We tried to cover a large phase space for grain size and porosity by an educated guess for the SPS parameters, by application of different mixing techniques (USB, USD, MOR), and by the use of pSi as base material. Indeed, only by using pSi we have been able to obtain and thus analyze samples of high porosity and large grain size, which we were not able to synthesize by the powder route.

We also tried to create sample pairs that allow for the direct comparison of a single variable change (e.g. SPS151 vs. SPS157 & SPS186 vs. SPS185 for mixing; SPS147 vs. SPS127 for temperature) and also densified all base-material powders and pSi without aluminum as a reference in order to see the effect of aluminum (see SPS40, SPS165, SPS193, SPS162, SPS237 in table S1).

Finally, from the analysis of all samples we find that the thermal conductivity in porous nanostructured silicon can be described by only three variables, namely domain size, interpore distance, and porosity. For the control of these parameters our study gives substantial information on the experimental variables and gives clear tendencies, even though a non-univariate variable set was chosen.
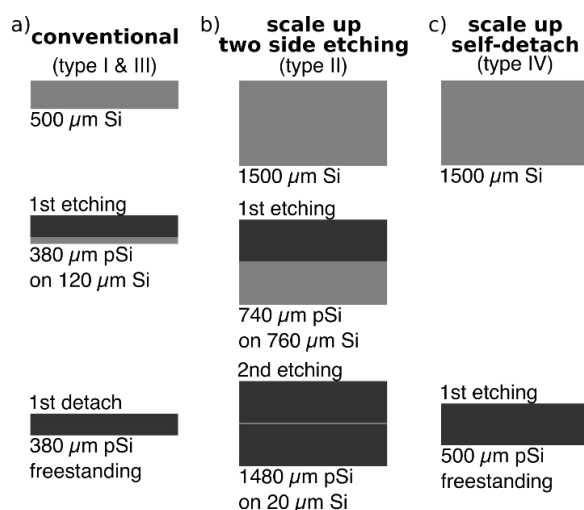

Figure S5 Schematics showing different pSi processing routes. Bright gray contrasts are used for bulk Si and dark gray is used for pSi. (a) A two-step process is applied to wafer type I & III. (b) Two side etching is applied for a 1500 μm thick wafer of type II. (c) The pSi membrane self-detached during the first etching.

Table S1 The table summarizes the set of experimental parameters and resulting sample parameters. Sorting is performed by the raw silicon material, the mixing procedure, the maximum sinter temperature, and the relative aluminum mass. The raw powder materials refer to 100 nm sized silicon nanoparticles, 18 nm sized aluminum particles while pSi parameters and etching parameters are summarized in Tab. 1 in the main text. Abbreviations in the mixing column are defined as USB : ultra sound bath, USD: ultra sound dispersion, MOR: mortaring. Classification of the morphology results from SEM images, the domain size and pore distance are analyzed from SEM top views.

SampleID	Raw Si	Raw Al	Al [%]	T_max [°C]	t min	mixing	Porosity [%]	Morphology	Domain size [m]	No. domains	pore-pore distance [m]	No. pores
	Experimental parameters						**Sample parameters**					
SPS40	powder	none	0	1000	5	none	12	particle	1.11E-07	1800	2.32E-07	11789
SPS165	powder	none	0	1200	10	none	2	grained	4.21E-06	4092	9.36E-07	448
SPS111	powder	powder	1	1000	5	USB	18	particle	1.16E-07	1283	2.31E-07	5981
SPS118	powder	powder	2	1000	5	USB	19	particle	9.57E-08	1840	1.74E-07	18893
SPS121	powder	powder	3	1000	5	USB	16	particle	1.04E-07	3151	2.32E-07	12404
SPS122	powder	powder	4	1000	5	USB	8	grained	3.36E-07	4824	4.30E-07	3021
SPS127	powder	powder	5	1000	5	USB	31	particle	9.42E-08	2366	1.77E-07	24664
SPS71	powder	powder	6	1000	5	USB	18	transient	1.38E-07	6982	3.14E-07	9283
SPS128	powder	powder	6	1000	5	USB	29	transient	1.33E-07	1089	2.02E-07	18261
SPS129	powder	powder	7	1000	5	USB	34	transient	1.20E-07	1578	2.76E-07	16143
SPS145	powder	powder	7	1000	5	USB	37	transient	1.28E-07	984	4.37E-07	4367
SPS77	powder	powder	10	1000	5	USB	9	grained	3.95E-07	6955	3.73E-07	2942
SPS151	powder	powder	4	1200	10	USB	13	grained	9.43E-07	2942	7.76E-07	4497
SPS147	powder	powder	5	1200	5	USB	11	grained	1.71E-06	2942	5.39E-07	2552
SPS157	powder	powder	4	1200	10	USD	4	grained	2.98E-07	6654	1.89E-06	2960
SPS160	powder	powder	5	1200	10	USD	4	grained	3.51E-07	8130	–	–
SPS177	powder	powder	20	1200	5	USD	1	grained	7.65E-07	5530	1.43E-06	8045
SPS204	powder	powder	20	1200	10	MOR	8	grained	4.14E-06	6658	5.37E-06	4858
SPS193	pSi(I)	none	0	1200	5	MOR	31	transient	2.33E-07	1627	8.35E-07	918
SPS194	pSi(I)	thin film	1	1200	5	MOR	29	transient	4.11E-07	3740	1.15E-06	5096
SPS195	pSi(I)	thin film	1	1200	5	MOR	29	transient	4.16E-07	5922	8.21E-07	14585
SPS162	pSi(II)	none	0	1200	10	USD	46	transient	9.70E-08	3266	3.12E-07	9823
SPS186	pSi(II)	powder	5	1200	5	MOR	46	transient	5.18E-08	1349	9.81E-08	5583
SPS185	pSi(II)	powder	5	1200	5	MOR+USD	50	transient	7.28E-08	2536	2.49E-07	12836
SPS237	pSi(III)	none	0	1200	5	MOR	16	grained	2.52E-07	3686	4.39E-07	6807
SPS202	pSi(IV)	powder	5	1200	5	MOR	19	grained	8.09E-08	7029	1.75E-07	15603

References

[S1] Grady, L. Random Walks for Image Segmentation. *IEEE Transactions on Pattern Analysis and Machine Intelligence* **2006**, *28*, 1768–1783.

[S2] Van der Walt, S. scikit-image: image processing in Python. *PeerJ* **2014**, *2*, e453.

[S3] J. Schindelin, I.; et al. Fiji: an open-source platform for biological-image analysis. *Nature Methods* **2012**, *9*, 676–682.

[S4] Legland, D; Arganda-Carreras, I.; Andrey P. MorphoLibJ: integrated library and plugins for mathematical morphology with ImageJ. *Bioinformatics* **2016**, *32*, 3532–3534.

[S5] Callaway, J. Model for Lattice Thermal Conductivity at Low Temperatures. *Phys. Rev.* **1959**, *113*, 1046–1051.

[S6] Jeong C.; Datta, S.; Lundstrom, M. Thermal conductivity of bulk and thin-film silicon: A Landauer approach. *Journal of Applied Physics* **2012**, *111*, 093708.

[S7] Hopcroft, M. A.; Nix, W. D.; Kenny, T. W. What is the Young's Modulus of Silicon?. *Journal of Microelectromechanical Systems* **2010**, *19*, 229–238.

[S8] Holland, M. G. Analysis of Lattice Thermal Conductivity. *Phys. Rev.* **1963**, *132*, 2461–2471.